Journal of Power Sources 245 (2014) 48–58

Contents lists available at SciVerse ScienceDirect

Journal of Power Sources

journal homepage: www.elsevier.com/locate/jpowsour

Lithium iron phosphate spheres as cathode materials for high power lithium ion batteries

Anh Vu, Andreas Stein*

Department of Chemistry, University of Minnesota, 207 Pleasant St. SE., Minneapolis, MN 55455, USA

HIGHLIGHTS

- $Li_3Fe_2(PO_4)_3$ nanospheres were fabricated by templating and calcination.
- Spherical $LiFePO_4$ particles embedded in carbon films were formed by spin casting.
- Both types of lithium iron phosphate spheres were tested as Li^+-battery cathodes.
- The spherical $Li_3Fe_2(PO_4)_3$ particles had a capacity of 100 mA h g^{-1} at 2.5 C rate.
- $LiFePO_4$/C composites had capacities of 130 and 50 mA h g^{-1} at C/2 and 16 C rates.

GRAPHICAL ABSTRACT

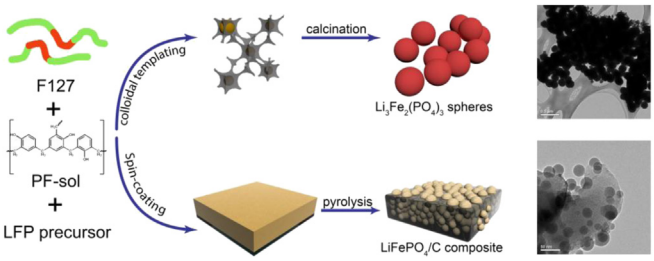

ARTICLE INFO

Article history:
Received 1 April 2013
Received in revised form
19 June 2013
Accepted 19 June 2013
Available online 28 June 2013

Keywords:
Colloidal crystal template
Lithium iron phosphate
Carbon nanocomposite
Lithium ion battery

ABSTRACT

Electrode materials composed of micrometer- and sub-micrometer-sized spherical particles are of interest for lithium ion batteries (LIBs) because spheres can be packed with higher efficiency than randomly shaped particles and achieve higher volumetric energy densities. Here we describe the synthesis of lithium iron phosphate (LFP) phases as cathode materials with spherical morphologies. Spherical $Li_3Fe_2(PO_4)_3$ particles and $LiFePO_4$ spheres embedded in a carbon matrix are prepared through phase separation of precursor components in confinement. Precursors containing Li, Fe, and P sources, pre-polymerized phenol–formaldehyde (carbon source), and amphiphilic surfactant (F127) are confined in 3-dimensional (colloidal crystal template) or 2-dimensional (thin film) spaces, and form spherical LFP particles upon heat treatment. Spherical $Li_3Fe_2(PO_4)_3$ particles are fabricated by calcining $LiFePO_4$/C composites in air at different temperatures. $LiFePO_4$ spheres embedded in a carbon matrix are prepared by spin-coating the LFP/carbon precursor onto quartz substrates and then applying a series of heat treatments. The spherical $Li_3Fe_2(PO_4)_3$ cathode materials exhibit a capacity of 100 mA h g^{-1} (83% of theoretical) at 2.5 C rate. $LiFePO_4$ spheres embedded in a carbon matrix have specific capacities of 130, 100, 83, and 50 mA h g^{-1} at C/2, 2 C, 4 C, and 16 C rates, respectively (PF_600_2), revealing excellent high-rate performance.

1. Introduction

Due to its low cost, environmental compatibility, and intrinsic thermal safety, lithium iron phosphate ($LiFePO_4$ or LFP) ranks among the most promising cathode materials for LIBs that target

* Corresponding author. Tel.: +1 612 624 1802; fax: +1 612 626 7541.
E-mail address: a-stein@umn.edu (A. Stein).

0378-7753/$ – see front matter © 2013 Elsevier B.V. All rights reserved.
http://dx.doi.org/10.1016/j.jpowsour.2013.06.116

the hybrid electric vehicle (HEV) and electric vehicle (EV) markets [1–4]. However, the low electronic and ionic conductivities of bulk LFP particles have restricted their rate performance, which is critical for HEV and EV power sources [5–8]. The electronic conductivity of LFP can be improved by coating it with carbon or metallic conductive layers [9–13]. The ionic conductivity can be boosted by doping with isovalent ions, and rate capabilities are improved by employing LFP nanoparticles [14]. The rate performance of LFP electrodes can be also improved by using nanoporous electrodes, because the interfacial area between a nanoporous electrode and the electrolyte is greatly increased [15–19]. Combinations of nanostructuring and conductive coatings increase the electronic and ionic conductivities simultaneously. 3DOM/m $LiFePO_4$/C composites with high surface areas, well-ordered structure, and good electronic conductivity have shown excellent rate performance (84 mA h g^{-1} at 5 C rate) [20]. Hierarchically porous $LiFePO_4$ and $LiFePO_4$/C composites have also been reported to exhibit very high rate performance [21–23]. The biggest disadvantage of using porous electrode materials is their low volumetric energy density, a point that will be addressed by the work described in this article.

The volumetric energy density of a battery is an important factor for electronic devices in which the available space for the power source is limited, such as portable devices. Electrodes composed of nanoparticles generally have good electrochemical performance (i.e., higher specific capacity and higher rate performance than electrodes composed of micron-sized particles) but low volumetric energy density as the nanoparticles are poorly packed. The volumetric energy density of an electrode depends strongly on its tap density, which is a macroscopic property that is affected by the morphology and the size of the bulk particles. In most cases, micrometer-sized particles have higher tap densities but worse electrochemical performance than particles with nanometer dimensions. For particles of similar size, the shape of the particles has a strong effect on tap density. Electrodes made of spherical particles normally have higher tap densities than those composed of irregular particles, as the spherical particles can be packed with higher efficiency [24–27]. One way to overcome the dilemma between electrochemical performance and tap density is to fabricate micron-sized spherical particles with nanometer-sized features, which are accessible to the electrolyte. Hollow $LiFePO_4$ spheres and porous $LiFePO_4$ microspheres have been fabricated for LIBs, and showed both high rate performance and high volumetric energy densities [28–30].

Carbon coatings are known to boost the electronic conductivity of LFP particles and also to limit the growth of LFP particles at high temperatures [21,31–36]. In the synthesis of 3DOM/m $LiFePO_4$/C composites mentioned above, the precursor was confined in the octahedral and tetrahedral sites of a face-centered cubic (fcc) colloidal crystal template (CCT) composed of close-packed, 400-nm PMMA spheres. As illustrated in Fig. 1, this resulted in the formation of a network of spherical $LiFePO_4$ particles that were connected through a carbon matrix [20]. If such nanospheres would be separated from the carbon matrix, they could be used as a cathode material with higher volumetric energy density while preserving the high rate performance of the original composite. Since in the CCT synthesis, the special interactions between $LiFePO_4$ precursor, phenol–formaldehyde (PF) sol, and surfactant inside the confining space of the template resulted in the formation of nano-spherical $LiFePO_4$ particles [20], we wondered if this would also be true for different types of confinement where growth is limited to two dimensions, such as in thin films. Here we describe syntheses of nano-spherical $Li_3Fe_2(PO_4)_3$ and $LiFePO_4$/C composites whose morphologies were influenced through the interplay between LFP precursor, PF sol, and amphiphilic surfactant inside confinement. $Li_3Fe_2(PO_4)_3$ was synthesized by calcining 3DOM/m $LiFePO_4$ composites in air to remove the carbon phase. Spherical $LiFePO_4$ particles embedded in a carbon matrix were synthesized by first spin-coating the precursor containing LFP-precursor, PF sol, and F127 in ethanol onto a quartz substrate and then pyrolyzing the aged composites under nitrogen. These syntheses are outlined in Fig. 1. Both approaches produced cathode materials that maintained high specific capacities (compared to the theoretical capacities) at high cycle rates with little loss over multiple cycles.

2. Experimental

2.1. Materials

The chemicals used in this study were obtained from the following sources: methyl methacrylate (MMA) monomer (99%), 2,2′-azobis(2-methyl propionamidine) dihydrochloride (AMPD) initiator (97%), concentrated aqueous H_3PO_4 solution (85 wt%), N-methyl-2-pyrrolidone (NMP) battery quality electrolyte (99.5%), polyvinylidene fluoride (PVdF), and lithium foil from Aldrich; Ketjenblack from AkzoNobel; lithium perchlorate (99.0%), ethylene carbonate (>99.0%), dimethyl carbonate (>99.0%) from Fluka; $FeCl_2 \cdot 4H_2O$ (98%), LiCl (99.5%), phenol (ACS reagent) and formaldehyde solution (37% aqueous solution) from Fisher Scientific; Pluronic F127 from BASF; hydrochloric acid (37%) from Malinckrodt Chemicals; and sodium carbonate (anhydrous, 99.7%) from J.T. Baker; 1 M $LiPF_6$ in ethylene carbonate–dimethyl carbonate–diethyl carbonate (EC–DMC–DEC, 4:3:3 vol. fractions, <50 ppm

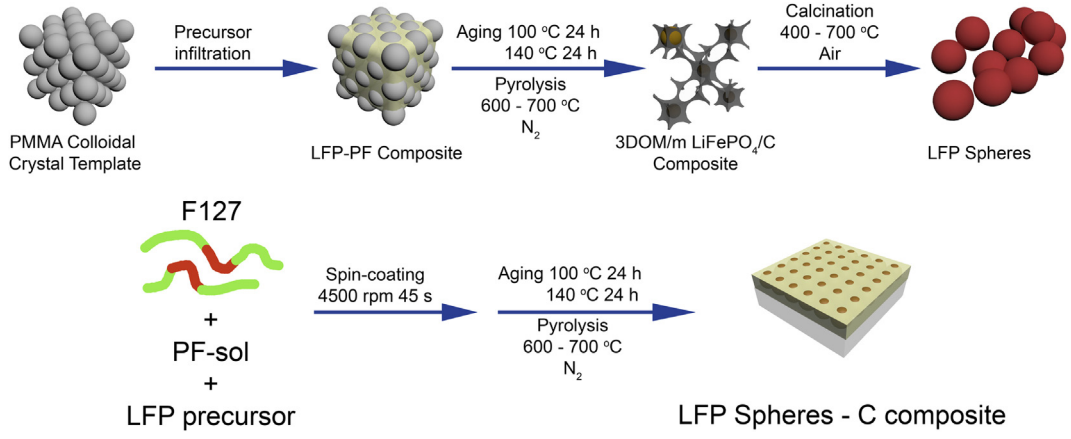

Fig. 1. Synthesis schemes to prepare LFP spheres and LFP sphere/C composites.

HF) from MTI Corporation. Deionized water was purified to a resistance higher than 18 MΩ.

2.2. Preparation of $Li_3Fe_2(PO_4)_3$ nanospheres

3DOM/m $LiFePO_4$/C composites were first prepared by a dual templating method according to a published procedure [20], in which the nonionic surfactant F127 (poly(ethylene oxide)–poly(propylene oxide)–poly(ethylene oxide) triblock copolymer $PEO_{106}PPO_{70}PEO_{106}$) and PMMA colloidal crystals were intended as templates for mesopores and macropores, respectively. PF-sol (2 g) was mixed with 2 g aqueous HCl (0.2 M) in a 20 mL vial and stirred for 15 min. F127 surfactant (1 g) was then added and stirred until a clear solution was obtained. $FeCl_2$ (1.988 g) and LiCl (0.435 g) were mixed and ground in a mortar, then transferred to the solution. The vial was placed in a larger glass bottle under flowing nitrogen to avoid the oxidation of Fe^{2+}. The mixture was stirred until all the salts were dissolved (usually 3–4 h, add 0.5 mL ethanol if the solution is too viscous), then concentrated H_3PO_4 (0.011 mol) was slowly added to the solution, and the mixture was stirred overnight. For template infiltration, several pieces of PMMA colloidal crystal templates were placed upright in a 20 mL vial, and the precursor solution was slowly added until the template pieces were partially immersed. The templates were infiltrated as a result of capillary forces. After 4 h, the infiltrated pieces were removed from the solution, gently touched with KimWipes™ paper tissue to wick away excess liquid, and then placed in a vacuum chamber for 30 min at room temperature. A second infiltration step was carried out following the same procedure. The samples were then placed in a vial that had been purged with nitrogen. The sealed vial was heated at 100 °C for 24 h, then at 140 °C for 24 h to increase the amount of cross-linking and to strengthen the composite. The aged composite samples were polished with 600 grit sand paper to remove nontemplated $LiFePO_4$ from the surface before pyrolysis. 3DOM/m $LiFePO_4$/C composites were obtained by pyrolyzing the thermally-cured composite under flowing N_2 (0.8 L min^{-1}) at 350 °C for 5 h and then at 600 °C for another 10 h with a heating rate of 1 °C min^{-1}. $Li_3Fe_2(PO_4)_3$ nanospheres were prepared by calcining the 3DOM/m $LiFePO_4$ composites in air at 400, 600, and 700 °C for 5 h with a heating rate of 1 °C min^{-1}.

2.3. Preparation of $LiFePO_4$/C composite nanospheres

Nanospherical $LiFePO_4$ was prepared by spin-coating LFP/C precursors on a quartz substrate at 4500 rpm for 45 s. Prepolymerized PF sol was prepared following an established method [37]. Briefly, phenol (61 g) was melted at 50 °C in a 500 mL round bottom flask using an oil bath. Under constant stirring, 13.6 g NaOH aqueous solution (20 wt%) was added slowly to the melted liquid over a period of 15 min. After that, 110.4 g aqueous formaldehyde solution (37 wt%) was added dropwise into the mixture. The solution was stirred at 500 rpm and heated at 70 °C for 1 h to increase the polymerization rate. The product was neutralized with 30 mL HCl (0.6 M), filtered to remove NaCl, and water was removed by vacuum evaporation at 50 °C overnight. The dried product was dissolved in 80 g ethanol to obtain the PF-sol, which was stored under refrigeration. Two different precursors with different amounts of PF sol were used. PF-sol (2 g or 1 g, 50 wt% in ethanol) was mixed with 2 g aqueous HCl (0.2 M) in a 20 mL vial and stirred for 15 min. F127 surfactant (1 g) was then added and stirred until a clear solution was obtained. $FeCl_2$ (1.988 g) and LiCl (0.435 g) were mixed and ground in a mortar, then transferred to the solution. At this point, the color of the solution changed from light yellow to green. The vial was placed in a larger glass bottle under flowing nitrogen to avoid the oxidation of Fe^{2+}. The mixture was vigorously stirred until all the salts were dissolved (usually 3–4 h). If the solution became too viscous for stirring, 0.5 mL ethanol was added. Then concentrated H_3PO_4 (0.011 mol) was slowly added to the solution, and the mixture was stirred overnight before being used for spin-coating. The spin-coated film was aged at 100 °C for 24 h, then at 140 °C for 24 h to increase the cross-linking of the polymer. The aged film was then stripped from the substrate and pyrolyzed at 600 or 700 °C for 5 h with a heating rate of 1 °C min^{-1} under nitrogen.

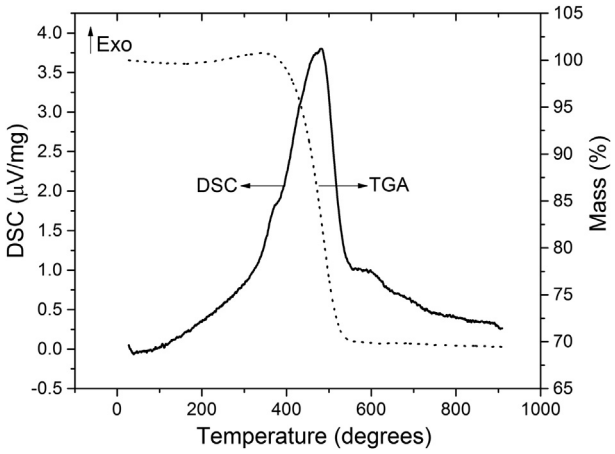

Fig. 2. TGA and DSC traces (obtained in air) of 3DOM/m $LiFePO_4$/C composites pyrolyzed at 600 °C.

2.4. Product characterization

All samples were ground into a fine powder before structural analyses. Product crystallinities and phase purities were determined by powder X-ray diffraction (XRD) using a PANalytical X-Pert PRO MPD X-ray diffractometer equipped with a cobalt source and an X-Celerator detector. Data were collected from 10° to 85° 2θ, at a step size of 0.017° and a rate of 20.7 s/step. Average crystallite sizes were estimated by Rietveld refinement using X'pert HighScore Plus 2.0a software. Instrumental broadening was corrected using a LaB_6 standard. Small-angle X-ray scattering (SAXS) data were acquired on a Rigaku RU-200BVH 2D SAXS instrument using a 12 kW-rotating anode with a Cu source and a Siemens Hi-Star multi-wire area detector. Raman spectroscopy was performed with a Witec Alpha300R confocal Raman microscope using 514.5 nm incident

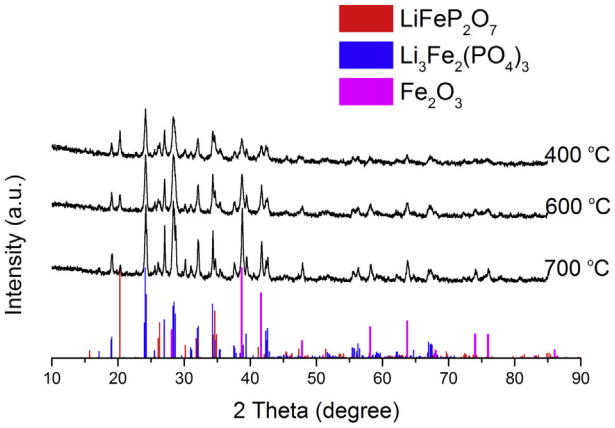

Fig. 3. XRD patterns of calcined 3DOM/m $LiFePO_4$/C composites at 400, 600 and 700 °C, showing $LiFeP_2O_7$, $Li_3Fe_2(PO_4)_3$, and Fe_2O_3 crystalline phases.

Table 1
XRD semi-quantitative analysis for $LiFeP_2O_7$, $Li_3Fe_2(PO_4)_3$, and Fe_2O_3 content based on their reference intensity rations (RIRs).

	400 °C	600 °C	700 °C
Fe_2O_3 (%)	6	9	11
$LiFeP_2O_7$ (%)	18	11	9
$Li_3Fe_2(PO_4)_3$ (%)	76	80	80

radiation at the lowest possible power to minimize beam damage of the sample. Scanning electron microscopy (SEM) was carried out with a JEOL-6700 microscope operating at 5 kV with emission currents ranging from 2 to 10 μA. Transmission electron microscopy (TEM) was carried out with a Technai T12 microscope operating at 120 kV with emission currents ranging from 7 to 12 μA. Thermogravimetric analysis (TGA) and differential scanning calorimetry (DSC) were performed on a Netzsch model STA 409 instrument to determine a suitable temperature program for the precursor transformation (flowing nitrogen atmosphere) and to determine the carbon content in the final products (flowing air atmosphere), using a heating rate of 5 °C min^{-1} to a final temperature of 900 °C.

2.5. Electrochemical tests

All electrochemical tests were carried out using an Arbin battery-testing system (ABTS 4.0). Galvanostatic charge–discharge measurements were performed in a coin cell, in which the spherical LFP materials (80 wt%) with 10 wt% carbon black and 10 wt% PVDf in NMP were used as the cathode and Li foil as the anode. The

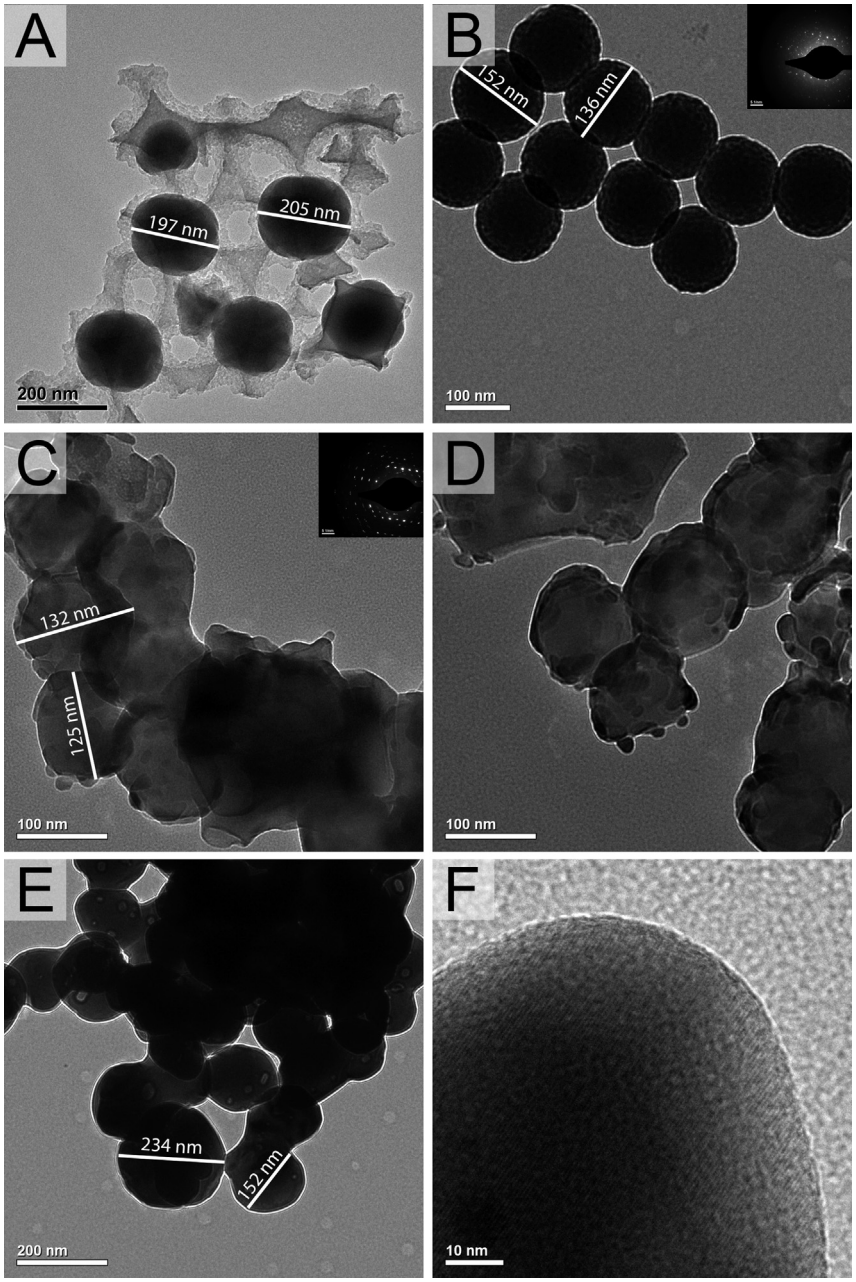

Fig. 4. TEM images of (A) 3DOM/m $LiFePO_4$/C composite, (B) $Li_3Fe_2(PO_4)_3$ prepared by calcining the $LiFePO_4$/C composite at 400 °C, (C, D) at 600 °C, and (E, F) at 700 °C. The insets in (B) and (C) show SA-ED patterns of the samples shown in the image.

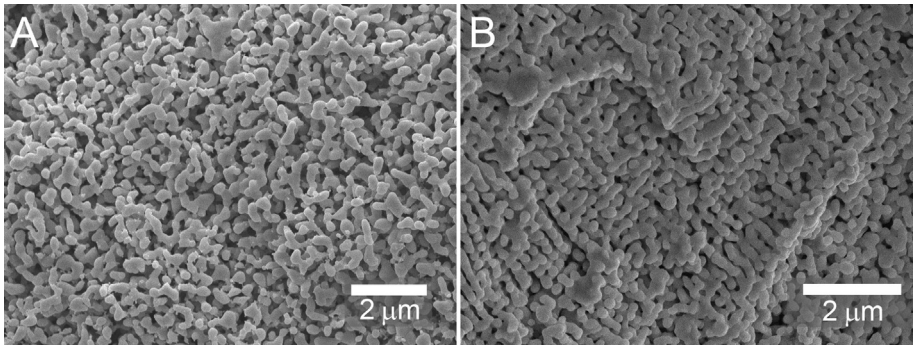

Fig. 5. SEM images of (A) $Li_3Fe_2(PO_4)_3$ calcined at 600 °C and (B) $Li_3Fe_2(PO_4)_3$ calcined at 700 °C, showing that spherical particles have sintered into longer particles.

electrolyte was 1 M $LiPF_6$ in EC–DMC–DEC solution. The cell was constructed and assembled in a dry room with <1% relative humidity. For cycling experiments, constant currents were applied and the voltages were restricted to a window of 2.0–4.2 V with 5 min rest periods between each step. All potential values are reported vs. Li/Li^+, and specific capacities are reported per gram of active material.

3. Results and discussion

3.1. $Li_3Fe_2(PO_4)_3$ nanospheres

In a previous publication [20], we described that 3DOM/m $LiFePO_4$/C composites were structured as spherical $LiFePO_4$ in octahedral sites connected by mesoporous carbon in tetrahedral sites. To obtain nano-spherical $LiFePO_4$ particles, the carbon phase must be removed. The easiest way to remove carbon is through combustion in air. A TGA trace of 3DOM/m $LiFePO_4$/C in air showed that the carbon phase was removed between 350 and 525 °C (Fig. 2). The amount of carbon in the sample was calculated from the TGA trace to be 30 wt% of the total mass.

It is well known that $LiFePO_4$ undergoes oxidation when heated in air at a temperature higher than 700 °C to give $Li_3Fe_2(PO_4)_3$ and Fe_2O_3, following the reaction [38,39]:

$$12LiFePO_4 + 3O_2 \rightarrow 4Li_3Fe_2(PO_4)_3 + 2Fe_2O_3$$

However, the XRD patterns of LFP obtained from the calcination of 3DOM/m $LiFePO_4$/C at different temperatures showed that the reaction actually happened at temperatures as low as 400 °C. When treated at 400 °C for 5 h, a dark red powder was obtained, indicating the presence of Fe_2O_3, which was confirmed by XRD of the obtained product. The fact that the reaction happened at lower temperatures can be attributed to the higher reactivity of nanosized $LiFePO_4$ and to the extra heat produced from carbon combustion, which creates local temperatures higher than the temperature set by the furnace. This made it impossible to remove carbon by calcination without affecting the $LiFePO_4$ phase. However, $Li_3Fe_2(PO_4)_3$, the main product of the oxidation reaction is another LFP electroactive phase with a theoretical capacity of 120 mA h g^{-1} and an average discharge voltage of 2.78 V, and it is also an attractive cathode material [38,39].

XRD characterization was used to investigate the products of oxidation of 3DOM/m $LiFePO_4$/C composites in air at 400, 600, and 700 °C. All XRD patterns showed three crystalline phases, $LiFeP_2O_7$, $Li_3Fe_2(PO_4)_3$, and Fe_2O_3 (Fig. 3). The fraction of each phase was calculated using the normalized reference intensity ratios (RIR) method since no other phases were detected in the XRD patterns of the calcined 3DOM/m $LiFePO_4$/C composites [40]. For the sample calcined at 400 °C, monoclinic $Li_3Fe_2(PO_4)_3$ contributed to 76% of the molar ratio of the mixture. The $LiFeP_2O_7$ crystalline phase was also observed for samples calcined at 600 or 700 °C, although its content became smaller as the calcination temperatures increased (Table 1). These data suggest that the oxidation reaction of 3DOM/m $LiFePO_4$/C composites in air may be a multi-step reaction, in which $LiFeP_2O_7$ is present as one of the intermediate phases and is then converted to $Li_3Fe_2(PO_4)_3$.

The effect of calcination temperature on morphologies of $Li_3Fe_2(PO_4)_3$ was investigated using SEM and TEM. Fig. 4A shows a TEM image of 3DOM/m $LiFePO_4$/C with the spherical $LiFePO_4$ phase in the carbon matrix before calcination, and Fig. 4B an image of $Li_3Fe_2(PO_4)_3$ particles after calcination at 400 °C. The sizes of the obtained $Li_3Fe_2(PO_4)_3$ spheres were smaller than the sizes of spherical $LiFePO_4$ in the carbon matrix, which may be attributed to

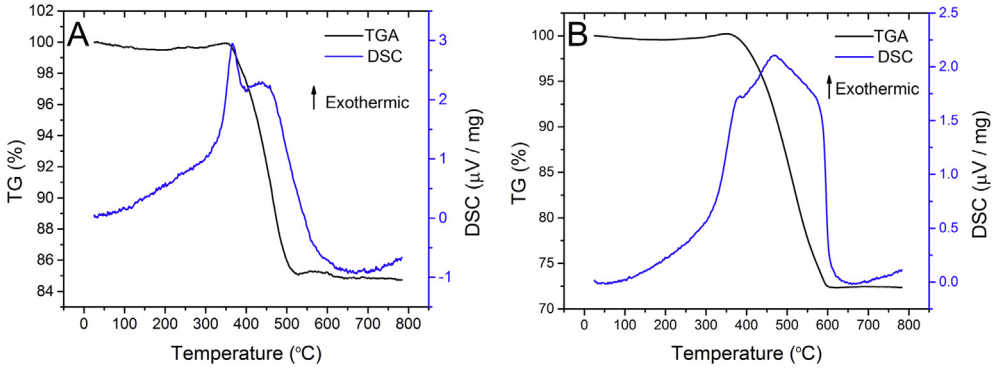

Fig. 6. TGA–DSC traces in air of samples made from (A) 1 g PF and (B) 2 g PF precursor.

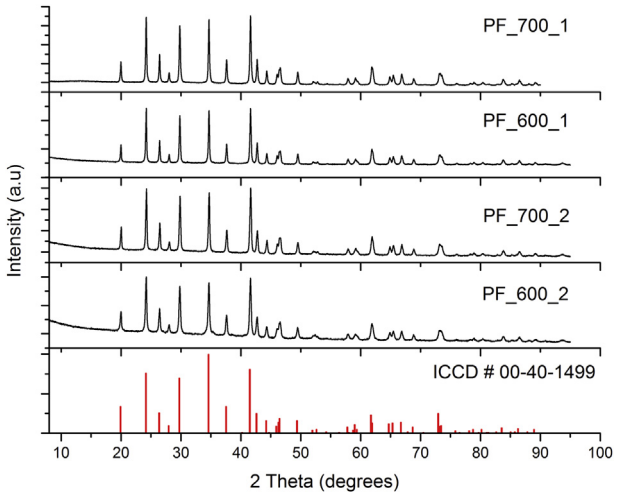

Fig. 7. XRD patterns of LFP/C composites, showing $LiFePO_4$ (ICCD#00-40-1499) as the only crystalline phase present.

loss of the carbon component and densification of the LFP phase. The sizes of these dense, crystalline spheres ranged from 132 nm to 155 nm, keeping diffusion paths for lithium ions relatively short during delithiation/lithiation processes (see below). The narrow range of sphere sizes enables a high packing efficiency and high volumetric capacity of electrodes prepared from these materials. For samples calcined at 600 and 700 °C, the sizes of isolated particles were even smaller, which indicates further condensation of the spheres at higher temperatures. In these samples, big particles were also observed that had formed from the aggregation of smaller particles. These aggregated particles were more noticeable in the sample calcined at 700 °C (Fig. 4E). The selected-area electron diffraction (SA-ED) patterns of samples calcined at 400 and 600 °C (insets in Fig. 4B and C) feature bright dots, which confirm the crystalline nature of these materials. The highly crystalline nature of these samples was also confirmed by lattice fringes shown in an image with higher magnification (Fig. 4F and Fig. S1 in Supplementary data). SEM images of the samples calcined at 600 and 700 °C show evidence for the aggregation and sintering of spherical particles into elongated particles (Fig. 5). The aggregation was more prominent in the sample calcined at 700 °C. These samples also feature small pores between particles, which can permit penetration of electrolyte inside the material. The elongated particles formed from the aggregation of 2–3 spherical particles, consistent with observations in the TEM images (Fig. 4C and D).

3.2. $LiFePO_4$/C nanosphere composites

Spherical $LiFePO_4$ is of interest for high volumetric energy density LIBs. The spherical shape in the LFP materials described above was achieved by confining the PF sol/LFP precursor in the interstitial sites of an fcc close-packed array of colloidal PMMA spheres. The sizes of the $LiFePO_4$ spheres depended on the volume of interstitial sites and, therefore, on the sizes of the colloidal polymer spheres. The colloidal crystal provided *three-dimensional* confinement. In the following part, we describe an investigation to determine whether it is possible to achieve spherical shapes of $LiFePO_4$ in *two-dimensional* confinement, such as in a thin film configuration.

Because two different precursors with different amounts of PF-sol were used, the samples were named according to the amount of PF in the precursors. For instance, the samples prepared from precursors containing 1 g PF and 2g PF and pyrolyzed at 600 °C were named PF_600_1 and PF_600_2, respectively. The different amounts of PF in the precursors were expected to produce composite materials with different contents of carbon. The TGA traces for samples pyrolyzed at 600 °C showed that the carbon content for samples made from 1 g PF and 2 g PF precursors was 15 and 28 wt%, respectively (Fig. 6).

The crystallinity of samples pyrolyzed at different temperatures was investigated using XRD. All samples produced diffraction patterns of $LiFePO_4$ (ICCD#00-40-1499) as the only crystalline phase; other crystalline impurities were not present or in such small quantities that they could not be detected by XRD (Fig. 7). A background signal between 8 and 30° 2Θ related to an amorphous carbon or polymer component was higher for the sample with the higher content of PF sol precursor (2 g) than for the sample with a lower content of PF precursor (1 g).

After spin-coating and aging at 100 and then at 140 °C, both precursors formed very homogeneous films (Fig. 8A). It was important to process the films by annealing immediately after spin-coating, otherwise micron-sized, spherical iron-rich particles formed within the polymeric network. Fig. 8B is the image of a film that was left at room temperature for 48 h before performing the annealing steps at 100 and 140 °C. The observation of dark aggregates in the film suggests that the mobility of iron species in the pre-polymerized solution is high, and that these species have a strong affinity for each other. Heat treatment accelerates the cross-linking of the pre-polymerized PF sol. Once a stable network is formed, it can prevent aggregation, as iron ions are now strongly bonded to phenol groups in the rigid network. A dark precipitate resulting from the chelation between phenol groups in the PF sol and iron ions was observed for the precursor solution after it had

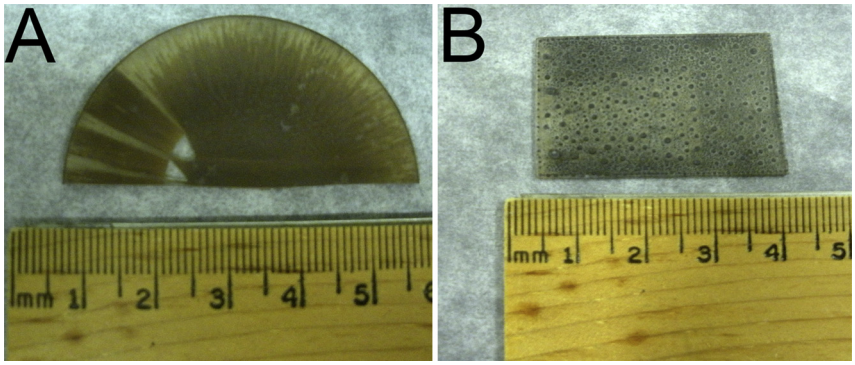

Fig. 8. Photographs of a $LiFePO_4$/C thin film composite (A) annealed at 100 °C immediately after spin-coating and then at 140 °C or (B) left in the atmosphere for 48 h without annealing.

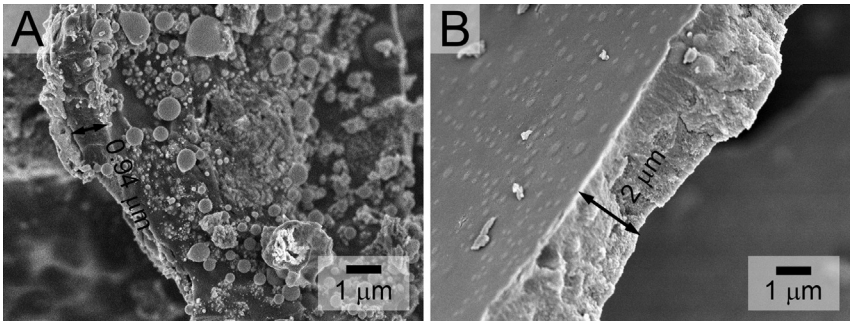

Fig. 9. SEM images of (A) PF_600_1 and (B) PF_600_2 $LiFePO_4$/C films that were used to estimate the film thickness.

been left for 2–3 days at room temperature. The chelation happened more quickly if F127 was not added to the solution. However, complexation leading to the formation of a precipitate in the solution is not desired, as it makes it impossible to cast homogeneous thin films.

Film morphologies of all samples were characterized using SEM and TEM. The film thicknesses were estimated from cross-sections of SEM images and were approximately 1 and 2 μm for samples prepared from 1 g and 2 g PF precursors, respectively (Fig. 9). The thicker films resulted from the higher viscosity of the precursor containing more PF.

The morphologies of $LiFePO_4$/C samples depended on both composition and pyrolysis temperatures. For samples with a lower carbon content, submicron to micron-sized spheres were found that protruded from the surfaces, whereas the surfaces of samples with a higher carbon content were smoother and contained smaller spheres (Figs. 9 and 10). In addition, after sample grinding, spheres were also found inside the film, which were much smaller than those on the surface of the film. The reason for this difference is the higher mobility of iron species on the surface compared to those inside the film, where they are restricted by the rigid polymer network. It is interesting that inside the films, smaller $LiFePO_4$ particles were embedded in a fibrous network. This fibrous, carbon-containing network effectively connects the $LiFePO_4$ particles, providing short, conductive paths for electrons. Higher pyrolysis temperatures created bigger spheres and more rugged film surfaces, while the fibrous phase did not seem to be affected by the temperature.

TEM images of PF_600_2 showed packed spherical $LiFePO_4$ particles inside a thin film (Figs. 11A,B and S3). Many nanocrystalline $LiFePO_4$ particles smaller than 10 nm were also observed inside the carbon matrix. The HRTEM image in Fig. 11B clearly shows the lattice fringes of such crystalline $LiFePO_4$ particles, which are different from the surrounding amorphous carbon phase. TEM images of PF_700_2 also showed the presence of spherical LFP particles embedded in a carbon matrix with particle sizes ranging from 10 to 150 nm (Fig. 11C and D). To summarize the structural information from SEM and TEM analyses, the 1–2 μm thick, spin-coated films were composed of nanospheres smaller than 350 nm, packed inside a fibrous carbon-containing matrix. On the surface of the films, spheres with sizes ranging from 0.7 to 1.5 μm were present. The carbon phase itself contained many randomly distributed nanocrystalline $LiFePO_4$ particles smaller than 10 nm. On the basis of a Raman spectral analysis, the crystallite size of

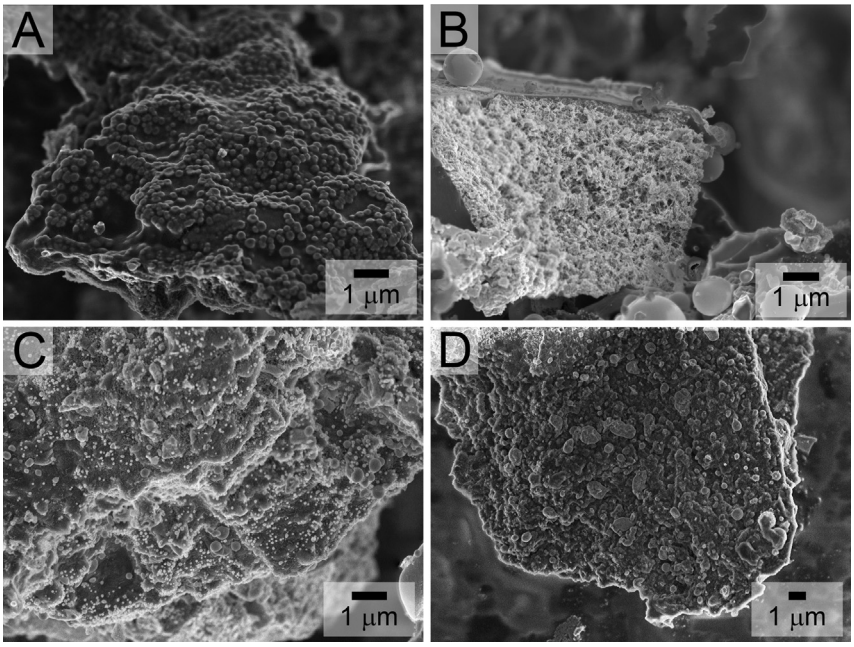

Fig. 10. SEM images of (A) PF_600_1 and (B) PF_700_1, showing microspheres protruding from the films and a fibrous phase. SEM images of (C) PF_600_2 and (D) PF_700_2, showing a smoother film surface with fewer microspheres protruding from the films.

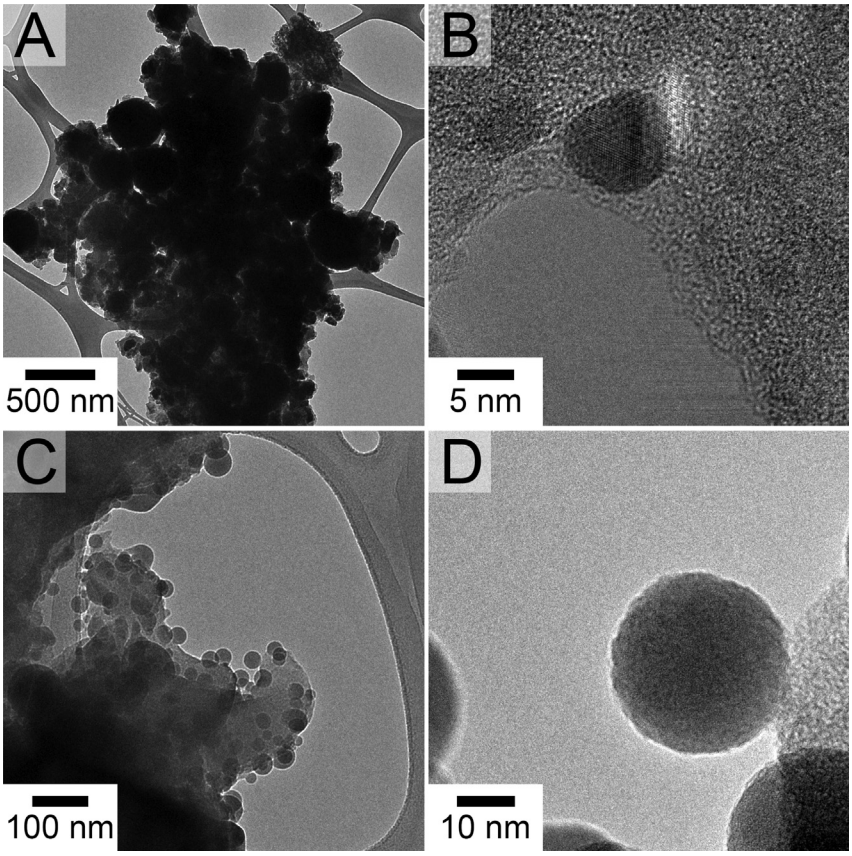

Fig. 11. TEM images of a $LiFePO_4$/C composite thin film made from 2 g PF precursor and pyrolyzed at (A, B) 600 °C or (C, D) 700 °C under nitrogen.

graphitic domains in the direction of graphitic planes was approximately 4.9 nm (Fig. S2).

3.3. Electrochemical tests

3.3.1. $Li_3Fe_2(PO_4)_3$ nanospheres

The discharge profile of a sample calcined at 600 °C shows two plateaus at 2.4 and 2.7 V (Fig. 12A), which are characteristic for the discharge profile of $Li_3Fe_2(PO_4)_3$ [41,42]. At slow rates (C/2), the specific discharge capacities for the samples calcined at 600 °C and 700 °C are 100 and 50 mA h g^{-1}, respectively (normalized to the actual weight percentage of $Li_3Fe_2(PO_4)_3$ in the sample). It is interesting that the capacity of the sample calcined at 600 °C is much higher than that of the sample calcined at 700 °C even though the two samples showed similar morphology and crystallinity. The capacity of the sample calcined at 600 °C is about 83% of the theoretical capacity, which is very promising for using this material for LIB cathodes. At different rates varying from C/2 to 2.5 C, the capacity of the sample calcined at 600 °C was retained while the capacity of the sample calcined at 700 °C continuously decreased. This may be attributed to the loss of surface area and the higher degree of aggregation of the sample calcined at 700 °C.

3.3.2. Spherical $LiFePO_4$/C composites

Electrochemical tests were performed with coin cells of spherical $LiFePO_4$/C composites. The cells were tested at different rates, ranging from C/2 to 16 C for many cycles. The discharge profiles of all samples showed the characteristic plateau of $LiFePO_4$ at 3.4 V

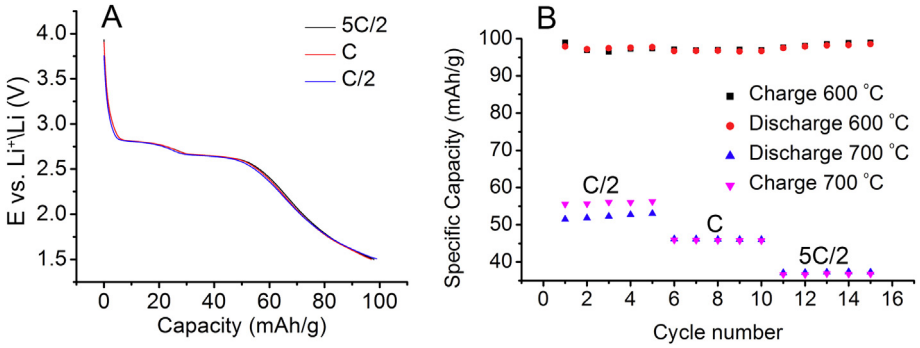

Fig. 12. (A) Discharge profile of $Li_3Fe_2(PO_4)_3$ calcined at 600 °C. (B) Cyclability of $Li_3Fe_2(PO_4)_3$ at different rates (C/2 for cycles 1–5, C for cycles 6–10, 5 C/2 for cycles 11–15).

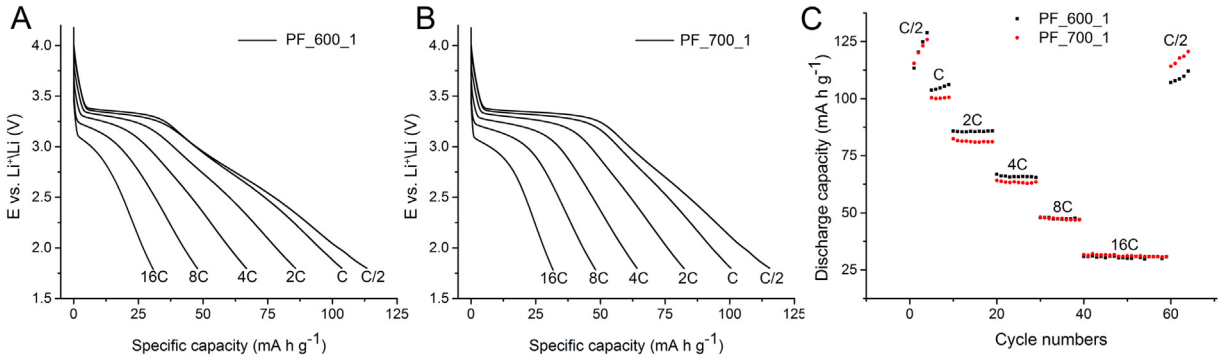

Fig. 13. (A, B) Discharge profiles and (C) rate performance of spherical $LiFePO_4$/C composites prepared from 1 g PF precursor and pyrolyzed at different temperatures.

(Fig. 13). The two samples prepared from 1 g PF precursor and with the lower carbon content (PF_600_1 and PF_700_1) showed similar performance. At a slow rate (C/2), both samples were able to deliver about 120 mA h g^{-1}, and at a higher rate (4 C) their discharge capacities were about 65 mA h g^{-1}. However, if we take a closer look at the discharge profiles of these samples, they are quite different. The sample pyrolyzed at 700 °C has more of its capacity delivered at 3.4 V, whereas a large portion of the capacity of the sample pyrolyzed at 600 °C is delivered at a lower potential. This means that even though both materials have the same lithium capacity, the sample pyrolyzed at 700 °C has a higher energy density. The plateau at 3.4 V is the characteristic potential for the intercalation of Li ions into the crystal lattice of $FePO_4$ forming $LiFePO_4$. The extraction of lithium ions at a lower potential (from 1.8 to 3.4 V) may originate from the removal of interfacial lithium ions at the $LiFePO_4$/carbon interfaces, where lithium ions are stored on the ionically conductive side (surface of $FePO_4$/$LiFePO_4$ particles) and electrons are localized on the electronically conductive side (surface of conductive carbon) [43]. Such interfacial lithium ion storage was also observed in several nanometer-sized transition metal oxides [44–46]. Here, the $LiFePO_4$/C film pyrolyzed at the lower temperature had larger average graphitic domain sizes and was able to store more lithium at the interfaces, so that more of its capacity was delivered at a lower potential. Both samples were able to operate at very high rate (16 C) and delivered about 32 mA h g^{-1} without fading for 20 cycles.

The electrochemical performance of the samples with higher carbon content was quite different and strongly depended on the pyrolysis temperature (Fig. 14). Samples pyrolyzed at lower temperatures (500 and 600 °C) were able to deliver 130 mA h g^{-1} at C/2

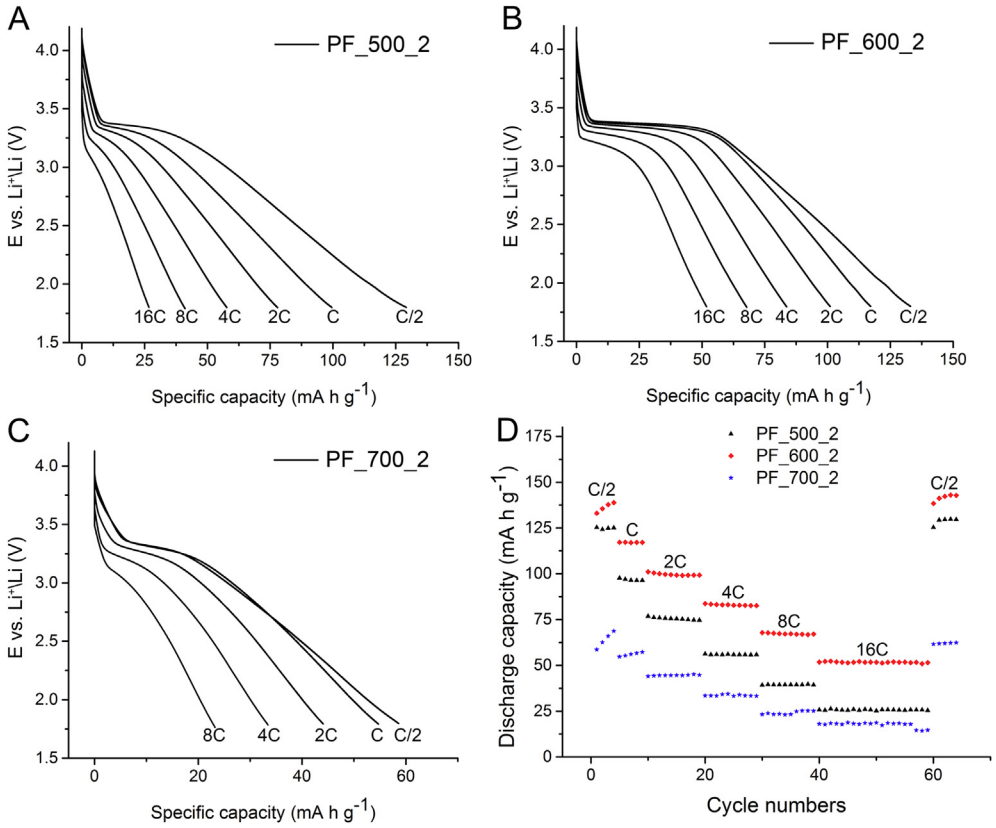

Fig. 14. Discharge profiles and rate performance of spherical $LiFePO_4$/C composites prepared from 2 g PF precursor and pyrolyzed at different temperatures.

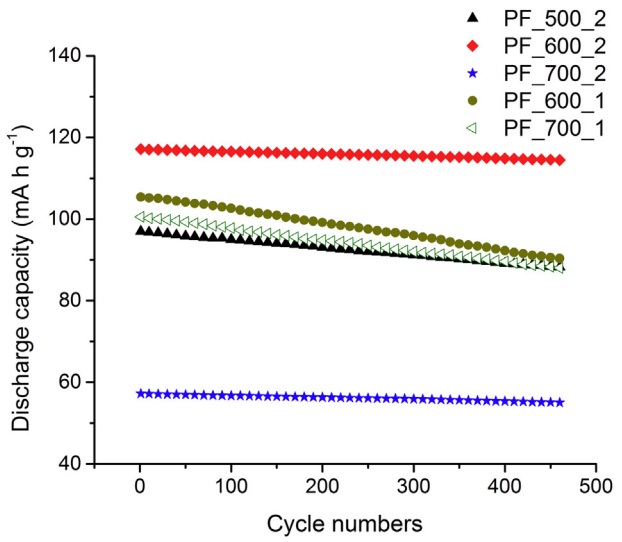

Fig. 15. Capacity retention of spherical $LiFePO_4$/C composites when cycled at 1 C.

rate, while the value for the sample pyrolyzed at 700 °C was only 60 mA h g^{-1}. This behavior was observed for multiple samples and was surprising, since the morphologies of the two samples pyrolyzed at 600 and 700 °C were quite similar, and no impurity phases were detectable by XRD for the sample pyrolyzed at 700 °C. It should be noted that only the PF_700_2 sample was unable to maintain the current when cycled at a 16 C rate; the other two samples cycled without any problems.

The amount of capacity delivered by the PF_600_2 sample at 3.4 V was higher than that of the PF_500_2 sample, the latter storing more lithium at the $LiFePO_4$/carbon interface, given the larger graphitic domains of PF_500_2 (Fig. S2). The PF_600_2 sample also had a better rate performance than the PF_500_2, particularly at higher rates. When cycled at a slow rate (C/2), both PF_600_2 and PF_700_2 samples showed increasing capacity over multiple cycles. During each cycle the sample gained about 2–5 mA h g^{-1}. This can be attributed to the presence of big LFP particles on the surface of the films, which needed more time for lithium ions to intercalate/deintercalate. This effect disappeared when the samples were cycled at high rates as the capacity contribution from the big $LiFePO_4$ particles at these rates was very limited. The PF_600_2 sample showed the best performance of all samples tested, with 130 mA h g^{-1} at C/2 rate and 50 mA h g^{-1} at 16 C rate. The good performance is attributed to the high carbon content and the small size and high crystallinity of the LFP phase that facilitated the diffusion of Li ions and the movement of electrons in the composite.

The cycle lives of the spherical $LiFePO_4$/C composites were studied by charging and discharging the materials at 1 C rate for more than 460 cycles (Fig. 15). All samples showed good stability with high capacity retention over many cycles. PF_600_2 sample exhibited the best capacity retention with only 2.3% capacity loss after 460 cycles and PF_600_1 the worst value with 14.3% capacity loss. It is interesting that the higher carbon content improved both the rate performance and the cycle life of these materials. The effect is attributed to the higher conductivity of the samples with higher carbon content.

4. Conclusions

LFP cathode materials are of great interest for HEV and EV applications. However, to be useful for portable devices, which require much higher volumetric energy density, the morphology of the electrode materials must be considered. Microspheres with nanometer-sized features are desirable because of their high tap density and typically good electrode performance. Here, two different approaches to obtain spherical LFP materials were described. Nano-spherical $Li_3Fe_2(PO_4)_3$ was obtained from the calcination of 3DOM/m $LiFePO_4$/C composites. The sample calcined at 600 °C showed good electrochemical performance with 100 mA h g^{-1} at 2.5 C rate and good cyclability. The cell capacity did not change when the rate was increased from C/5 to 2.5 C, and even at very high rate (2.5 C) the capacity was maintained after 50 cycles. However, a disadvantage of this material is the presence of Fe_2O_3 as a non-reactive phase, which decreases its specific capacity.

$LiFePO_4$/C composites prepared by spin-casting contained $LiFePO_4$ nanospheres in a carbon matrix and showed very good electrochemical performance, i.e., relatively high specific capacities and high rate capabilities. Materials that had been pyrolyzed at 500 or 600 °C were able to maintain a current when cycled at very high rates (up to 16 C). The capacity contributions at various potentials depended on the nature of the carbon phase in the composite electrodes. Materials pyrolyzed at 500 °C (PF_500_2) contained a carbon phase with larger graphitic domains and showed a higher capacity contribution at lower potentials, which was ascribed to lithium storage at the interface formed between LFP and carbon. Samples pyrolyzed at higher temperatures had most of their capacity delivered at a higher potential (3.4 V). The best performance was observed for a sample pyrolyzed at 600 °C with 72 wt% of $LiFePO_4$ spheres and 28 wt% of carbon, which delivered 130 mA h g^{-1} at C/2 rate and 100 mA h g^{-1} at 2 C rate.

Acknowledgments

This material is based upon work that was supported by the Department of Energy Office of Science under Award Number DE-SC0008662. Parts of this work were carried out in the University of Minnesota Characterization Facility, which receives partial support from the NSF through the MRSEC, ERC, MRI, and NNIN programs. We thank Professor William H. Smyrl for access to his dry room and electrochemical equipment and Professor R. Lee Penn for use of her powder X-ray diffractometer.

Appendix A. Supplementary data

Supplementary data associated with this article can be found in the online version, at http://dx.doi.org/10.1016/j.jpowsour.2013.06.116.

References

[1] J. Axsen, K.S. Kurani, A. Burke, Transport Policy 17 (2010) 173–182.
[2] J.B. Goodenough, Y. Kim, Chem. Mater. 22 (2010) 587–603.
[3] L.-X. Yuan, Z.-H. Wang, W.-X. Zhang, X.-L. Hu, J.-T. Chen, Y.-H. Huang, J.B. Goodenough, Energy Environ. Sci. 4 (2011) 269–284.
[4] M.S. Whittingham, Y. Song, S. Lutta, P.Y. Zavalij, N.A. Chernova, J. Mater. Chem. 15 (2005) 3362–3379.
[5] C. Delacourt, P. Poizot, J.-M. Tarascon, C. Masquelier, Nat. Mater. 4 (2005) 254–260.
[6] C. Delmas, M. Maccario, L. Croguennec, F. Le Cras, F. Weill, Nat. Mater. 7 (2008) 665–671.
[7] B. Kang, G. Ceder, Nature 458 (2009) 190–193.
[8] S.-I. Nishimura, G. Kobayashi, K. Ohoyama, R. Kanno, M. Yashima, A. Yamada, Nat. Mater. 7 (2008) 707–711.
[9] Z. Chen, J.R. Dahn, J. Electrochem. Soc. 149 (2002) A1184–A1189.
[10] R. Dominko, M. Bele, M. Gaberscek, M. Remskar, D. Hanzel, S. Pejovnik, J. Jamnik, J. Electrochem. Soc. 152 (2005) A607–A610.
[11] Y.S. Hu, Y.G. Guo, R. Dominko, M. Gaberscek, J. Jamnik, J. Maier, Adv. Mater. 19 (2007) 1963–1966.
[12] H.-T. Chung, S.-K. Jang, H.W. Ryu, K.-B. Shim, Solid State Commun. 131 (2004) 549–554.

[13] S.-A. Hong, S.J. Kim, J. Kim, B.G. Lee, K.Y. Chung, Y.-W. Lee, Chem. Eng. J. 198-199 (2012) 318–326.
[14] S.-Y. Chung, J.T. Bloking, Y.-M. Chiang, Nat. Mater. 1 (2002) 123–128.
[15] G. Hasegawa, Y. Ishihara, K. Kanamori, K. Miyazaki, Y. Yamada, K. Nakanishi, T. Abe, Chem. Mater. 23 (2011) 5208–5216.
[16] I. Moriguchi, S. Nabeyoshi, M. Izumi, H. Yamada, Chem. Lett. 41 (2012) 1639–1641.
[17] T. Nakamura, Y. Shima, H. Matsui, Y. Yamada, S. Hashimoto, H. Miyauchi, N. Koshiba, J. Electrochem. Soc. 157 (2010) A544–A549.
[18] S. Bodoardo, C. Gerbaldi, G. Meligrana, A. Tuel, S. Enzo, N. Penazzi, Ionics 15 (2009) 19–26.
[19] N. Penazzi, S. Bodoardo, R. Bongiovanni, C. Gerbaldi, G. Meligrana, G. Mulas, J. Nair, Fuel Cells 9 (2009) 273–276.
[20] A. Vu, A. Stein, Chem. Mater. 23 (2011) 3237–3245.
[21] C.M. Doherty, R.A. Caruso, B.M. Smarsly, P. Adelhelm, C.J. Drummond, Chem. Mater. 21 (2009) 5300–5306.
[22] C.M. Doherty, R.A. Caruso, B.M. Smarsly, C.J. Drummond, Chem. Mater. 21 (2009) 2895–2903.
[23] J.C. Badot, É. Ligneel, O. Dubrunfaut, D. Guyomard, B. Lestriez, Adv. Funct. Mater. 19 (2009) 2749–2758.
[24] J. Gao, J. Ying, C. Jiang, C. Wan, J. Power Sources 166 (2007) 255–259.
[25] J.-F. Ni, H.-H. Zhou, J.-T. Chen, X.-X. Zhang, Mater. Lett. 61 (2007) 1260–1264.
[26] J.-R. Ying, M. Lei, C.-Y. Jiang, C. Wan, X. He, J. Li, L. Wang, J. Ren, J. Power Sources 158 (2006) 543–549.
[27] J. Ying, C. Wan, C. Jiang, Y. Li, J. Power Sources 99 (2001) 78–84.
[28] C. Sun, S. Rajasekhara, J.B. Goodenough, F. Zhou, J. Am. Chem. Soc. 133 (2011) 2132–2135.
[29] J. Liu, T.E. Conry, X. Song, M.M. Doeff, T.J. Richardson, Energy Environ. Sci. 4 (2011) 885–888.
[30] M.H. Lee, J.Y. Kim, H.K. Song, Chem. Commun. 46 (2010) 6795–6797.
[31] Y. Wang, E. Hosono, K. Wang, H. Zhou, Angew. Chem., Int. Ed. 47 (2008) 7461–7465.
[32] Y. Liu, D. Liu, Q. Zhang, D. Yu, J. Liu, G. Cao, Electrochim. Acta 56 (2010) 2559–2565.
[33] K. Wang, R. Cai, T. Yuan, X. Yu, R. Ran, Z. Shao, Electrochim. Acta 54 (2009) 2861–2868.
[34] X. Zhi, G. Liang, L. Wang, X. Ou, L. Gao, X. Jie, J. Alloys Compd. 503 (2010) 370–374.
[35] Y.-D. Cho, G.T.-K. Fey, H.-M. Kao, J. Power Sources 189 (2009) 256–262.
[36] Y. Lin, M.X. Gao, D. Zhu, Y.F. Liu, H.G. Pan, J. Power Sources 184 (2008) 444–448.
[37] Y. Meng, D. Gu, F. Zhang, Y. Shi, H. Yang, Z. Li, C. Yu, B. Tu, D. Zhao, Angew. Chem., Int. Ed. 44 (2005) 7053–7059.
[38] M. Sato, S. Tajimi, H. Okawa, K. Uematsu, K. Toda, Solid State Ionics 152–153 (2002) 247–251.
[39] H.Z.S. Zhu, T. Miyoshi, M. Hibino, I. Honma, M. Ichihara, Adv. Mater. 16 (2004) 2012–2017.
[40] F.H. Chung, J. Appl. Crystallogr. 7 (1974) 519–525.
[41] A.K. Padhi, K.S. Nanjundaswamy, J.B. Goodenough, J. Electrochem. Soc. 144 (1997) 1188–1194.
[42] C. Masquelier, A.K. Padhi, K.S. Nanjundaswamy, J.B. Goodenough, J. Solid State Chem. 135 (1998) 228–234.
[43] X.-L. Wu, L.-Y. Jiang, F.-F. Cao, Y.-G. Guo, L.-J. Wan, Adv. Mater. 21 (2009) 2710–2714.
[44] J. Maier, Nat. Mater. 4 (2005) 805–815.
[45] P. Balaya, H. Li, L. Kienle, J. Maier, Adv. Funct. Mater. 13 (2003) 621–625.
[46] J. Jamnik, J. Maier, Phys. Chem. Chem. Phys. 5 (2003) 5215–5220.